letters to nature

(1 × 1) surface unit cell. For the interfaces we used a grid corresponding to 16 k-points per (1 × 1) unit cell. For metallic structures we used the Mermin functional with a temperature of 1,000 K and the extrapolation to zero Kelvin proposed in ref. 28.

The band offsets have been derived by relating the plane wave part of the potential, averaged laterally, to band edges. The relative displacement between potential and band edges has been obtained from the epitaxially strained bulk materials.

The phase diagram in Fig. 2 was obtained from the total energies as a function of the oxygen chemical potential. A number of different, stoichiometric and non-stoichiometric, interface structures with varying oxygen content have been considered. The regions where one of the stoichiometric interfaces (A, B or the dimer-oxidized variant of B) is most stable are shaded. Tests for the upper boundary of interface A with larger, that is (4 × 4), unit cells confirmed that the phase boundaries obtained in (2 × 2) unit cell are reliable to about 0.03 eV.

1. Moore, G. E. Cramming more components onto integrated circuits. *Electronics* **38**, 114–117 (1965).
2. Semiconductor Industry Association. *International Technology Roadmap for Semiconductors* at ⟨http://public.itrs.net/⟩ (International SEMATECH, Austin, TX, 2001).
3. Ishiwara, H. & Azuma, K. Oriented growth of SrTiO₃ films on Si(100) substrates using in-situ cleaning by excited hydrogen. *Mater. Res. Soc.* **116**, 369–374 (1988).
4. Kado, Y. & Arita, Y. Heteroepitaxial growth of SrO films on Si substrates. *J. Appl. Phys.* **61**, 2398–2400 (1987).
5. Mori, H. & Ishiwara, H. Epitaxial growth of SrTiO₃ films on Si(001) substrates using a focused electron beam evaporation method. *J. Appl. Phys.* **30**, 1415–1417 (1991).
6. Kim, T. W. *et al.* Structural properties and interfacial layer formation mechanisms of PbTiO₃ thin films grown on p-Si substrates. *Appl. Phys. Lett.* **64**, 2676–2678 (1994).
7. Alexe, M. Measurement of interface trap states in metal ferroelectric silicon heterostructures. *Appl. Phys. Lett.* **72**, 2283–2285 (1998).
8. McKee, R. A., Walker, F. J. & Chisholm, M. F. Crystalline oxides on silicon: the first five monolayers. *Phys. Rev. Lett.* **81**, 3014–3017 (1998).
9. McKee, R.A. & Walker, F.J. Process for depositing an oxide epitaxially onto a silicon substrate and structures prepared with the process. US patent 5,225,031 (United States Patent Office, 1993).
10. McKee, R. A., Walker, F. J. & Chisholm, M. F. Physical structure and inversion charge at a semiconductor interface with a crystalline oxide. *Science* **293**, 468–471 (2001).
11. Ashman, C., Först, C. J., Schwarz, K. & Blöchl, P. E. First-principles calculations of strontium adsorption on Si(001). *Phys. Rev. B* **69** (in the press).
12. Fan, W. C., Wu, N. J. & Ignatiev, A. Observation of ordered structures of Sr on the Si(001) surface. *Phys. Rev. B* **42**, 1254–1257 (1990).
13. Yao, X. *et al.* Initial stages of Ba adsorption on the Si(100)-(2 × 1) surface at room temperature. *Phys. Rev. B* **59**, 5115–5119 (1999).
14. Wang, J. *et al.* Bonding and diffusion of Ba on a Si(001) reconstructed surface. *Phys. Rev. B* **60**, 4968–4971 (1999).
15. Liang, Y., Gan, S. & Engelhard, M. First step towards the growth of single-crystal oxides on Si: formation of a two-dimensional crystalline silicate on Si(001). *Appl. Phys. Lett.* **79**, 3591–3593 (2001).
16. Wang, J., Ooms, W. J. & Hallmark, J. A. Semiconductor structure having a crystalline alkaline earth metal oxide interface with silicon. US patent 6,238,459 (United States Patent Office, 2001).
17. Droopad, R. *et al.* Epitaxial oxides on silicon grown by molecular beam epitaxy. *J. Cryst. Growth* **227–228**, 936–943 (2001).
18. Robertson, J. & Peacock, P. W. Atomic structure, band offsets and hydrogen in high k oxide:silicon interfaces. *Mater. Res. Soc. Symp. Proc.* **747**, 99–111 (2002).
19. Zhang, X., Demkov, A. A., Li, H., Hu, X. & Wei, Y. Atomic and electronic structure of the Si/SrTiO₃ interface. *Phys. Rev. B* **68**, 125323 (2003).
20. Chambers, S. A. *et al.* Band offset and structure of SrTiO₃/Si(001) heterojunctions. *J. Vac. Sci. Technol. A* **19**, 934–939 (2001).
21. Robertson, J. Band offsets of wide-band-gap oxides and implications for future electronic devices. *J. Vac. Sci. Technol. B* **18**, 1785–1791 (2000).
22. Hohenberg, P. & Kohn, W. Inhomogeneous electron gas. *Phys. Rev. B* **136**, 864–871 (1964).
23. Kohn, W. & Sham, L. J. Self-consistent equations including exchange and correlation effects. *Phys. Rev. A* **140**, 1133–1138 (1965).
24. Noland, T. A. Optical absorption of single-crystal strontium titanate. *Phys. Rev.* **94**, 724 (1954).
25. Car, R. & Parrinello, M. Unified approach for molecular dynamics and density-functional theory. *Phys. Rev. Lett.* **55**, 2471–2474 (1985).
26. Perdew, J. P., Burke, K. & Ernzerhof, M. Generalized gradient approximation made simple. *Phys. Rev. Lett.* **77**, 3865–3868 (1996).
27. Blöchl, P. E. Projector augmented-wave method. *Phys. Rev. B* **50**, 17953–17979 (1994).
28. Gillan, M. G. Calculation of the vacancy formation energy in aluminium. *J. Phys. Condens. Matter* **1**, 689–711 (1989).

High-latitude controls of thermocline nutrients and low latitude biological productivity

J. L. Sarmiento[1], N. Gruber[2], M. A. Brzezinski[3] & J. P. Dunne[4]

[1]*Atmospheric and Oceanic Sciences Program, Princeton University, Princeton, New Jersey 08544, USA*
[2]*IGPP and Department of Atmospheric Sciences, University of California at Los Angeles, Los Angeles, California 90095, USA*
[3]*Department of Ecology, Evolution and Marine Biology and the Marine Science Institute, University of California, Santa Barbara, California 93106, USA*
[4]*NOAA/Geophysical Fluid Dynamics Laboratory, PO Box 308, Forrestal Campus B Site, Princeton, New Jersey 08542, USA*

The ocean's biological pump strips nutrients out of the surface waters and exports them into the thermocline and deep waters. If there were no return path of nutrients from deep waters, the biological pump would eventually deplete the surface waters and thermocline of nutrients; surface biological productivity would plummet. Here we make use of the combined distributions of silicic acid and nitrate to trace the main nutrient return path from deep waters by upwelling in the Southern Ocean[1] and subsequent entrainment into subantarctic mode water. We show that the subantarctic mode water, which spreads throughout the entire Southern Hemisphere[2,3] and North Atlantic Ocean[3], is the main source of nutrients for the thermocline. We also find that an additional return path exists in the northwest corner of the Pacific Ocean, where enhanced vertical mixing, perhaps driven by tides[4], brings abyssal nutrients to the surface and supplies them to the thermocline of the North Pacific. Our analysis has important implications for our understanding of large-scale controls on the nature and magnitude of low-latitude biological productivity and its sensitivity to climate change.

The classical explanation for the observed nutrient distribution of the ocean in the low latitudes is that the downward flux of biogenic material from the surface of the ocean is balanced by upwelling of dissolved inorganic nutrients driven by vertical mixing in the main thermocline. This essentially one-dimensional view grew out of early theories of thermocline and thermohaline circulation that are no longer tenable. Estimates of the magnitude of vertical mixing in the main thermocline are about an order of magnitude smaller than required to explain the vertical profiles of tracers within this feature[5]. In addition, ocean model simulations of radiocarbon distribution show that balancing the formation of deep waters by upwelling through the main thermocline gives results that are inconsistent with observations[1]. Instead, these studies suggest that a more likely return path for the deep water to the surface is in the Southern Ocean[1].

Subantarctic Mode Water (SAMW) has been identified as the main conduit of nutrients from the Southern Ocean to the upwelling regions of the equatorial Pacific and off South America[6]. The SAMW is a pycnostad (a layer of relatively uniform density) that originates in the thick wintertime mixed layers that ring the Southern Ocean[7] (Fig. 1d). This belt, which is particularly strong eastward of the central Indian Ocean to the western South Atlantic, coincides with the Subantarctic Zone (SAZ) between the Subtropical Front at about 40–45° S and the Subantarctic Front at about 45–55° S, and appears to also include the Polar Front Zone (PFZ) between the Subantarctic Front and Polar Front just to the south (Fig. 1d). The SAMW pycnostad increases in density from $\sigma_\theta = 26.5$ (equivalent to 1,026.5 kg m^{-3}) in the western Atlantic to $\sigma_\theta = 27.1$ in the southeast Pacific[8] as it flows in an eastward circuit around the Southern Ocean.

One unusual characteristic of the waters found in this band is that they have high concentrations of nitrate (Fig. 1a), but low concentrations of silicic acid (Fig. 1b). We define a new tracer, $Si^* = [Si(OH)_4] - [NO_3^-]$, whose concentrations of $-10\,\mu mol\,kg^{-1}$ to $-15\,\mu mol\,kg^{-1}$ in the SAMW formation regions (Fig. 1c) are the lowest we were able to find anywhere at the surface of the ocean. We use the low Si* characteristic to trace the SAMW on the $\sigma_\theta = 26.8$ surface, which is the median of the range of densities that make up the SAMW (Si* is nearly conserved in this water mass; see Methods). Figure 2a charts the reach of low-Si* SAMW throughout the Southern Hemisphere subtropical gyres[2] and into the North Atlantic, where it is part of the upper water return flow of the global thermohaline circulation[3].

In addition to being a powerful water mass tracer, Si* is an indicator of nutrient status related to the requirements of diatoms. Diatoms with adequate light and nutrients (including iron) generally contain Si and N in a mole ratio of ~1:1 (ref. 9), which requires $Si^* \gtrsim 0$. The presence of negative-Si* SAMW waters at the base of the main thermocline (see depth in Fig. 2b) is associated with a silicic acid:nitrate ratio of ≤ 0.5 in the supply to surface waters (Fig. 2c; see Methods), which helps explain the prevalence of low diatom production over much of the world ocean[9].

High nutrients in the surface waters of the Southern Ocean where SAMW forms cause this water type to be a significant source of nutrients to the rest of the ocean. To evaluate the influence of this supply on biological productivity in the rest of the ocean, we performed a simulation with an ocean biogeochemistry general circulation model in which the Southern Ocean nutrient source was turned off by forcing nutrients towards zero at the surface of the ocean south of 30° S (see Methods). A comparison of this simulation to one in which surface nutrients were forced to observations everywhere suggests that the Southern Ocean nutrient supply accounts for about three-quarters of the biological production north of 30° S (Fig. 3).

The North Pacific Ocean is an important exception to the dominance of the SAMW influence. Figure 2a indicates that the main thermocline must be tapping directly into the high-nutrient waters of the deep ocean in this region[10]. The northernmost region of this basin is an area of upwelling; and wintertime cooling can make the water quite dense at the surface, particularly in the Sea of Okhotsk. The densest waters at the surface in the Sea of Okhotsk are only about $\sigma_\theta = 26.8$ (ref. 11), which is not high enough to allow deep waters to reach the surface. However, $\sigma_\theta = 26.8$ is the median density of upper North Pacific Intermediate Water[12] (NPIW), the formation of which is the result of a complex series of processes occurring in the Sea of Okhotsk[4,13] (probably involving strong vertical mixing driven by tidal interactions in the Kurile Islands[4,14]), as well as processes occurring in the 'mixed water region' between the Kuroshio and Oyashio currents[12,15]. We suggest that the strong vertical mixing in the Kurile Islands region brings deep nutrients up into the thermocline at the depth of the NPIW as well as above it.

The influence of NPIW extends over the entire North Pacific to
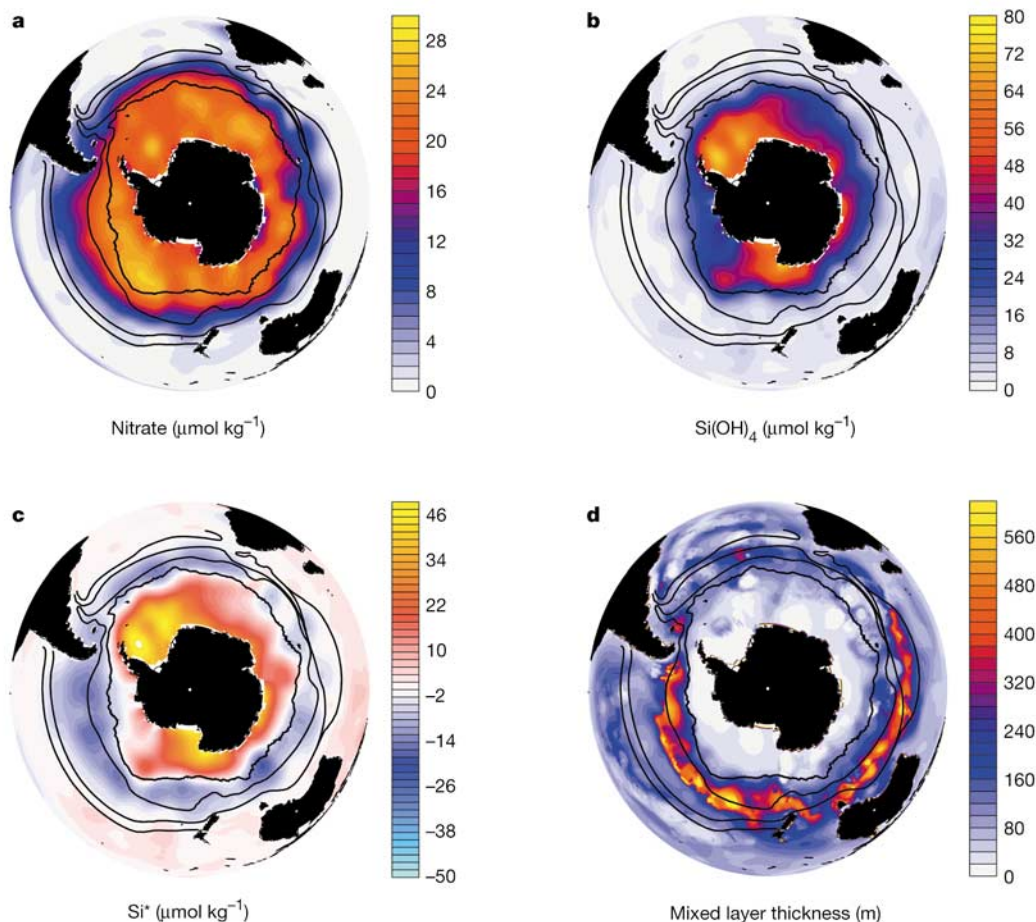
Figure 1 Polar stereographic maps of upper ocean nutrients and physics. **a**, Annual mean nitrate; **b**, annual mean silicic acid; **c**, annual mean Si*; and **d**, winter mixed layer thickness averaged over the July–September period. The southerly line denotes the mean position of the Polar Front[26]. In sequence from south to north, the remaining lines denote the position of the Subantarctic Front, the Southern Subtropical Front, and the Northern Subtropical Front[27]. Nutrient data are from ref. 28; the mixed layer thickness data are from ref. 29.
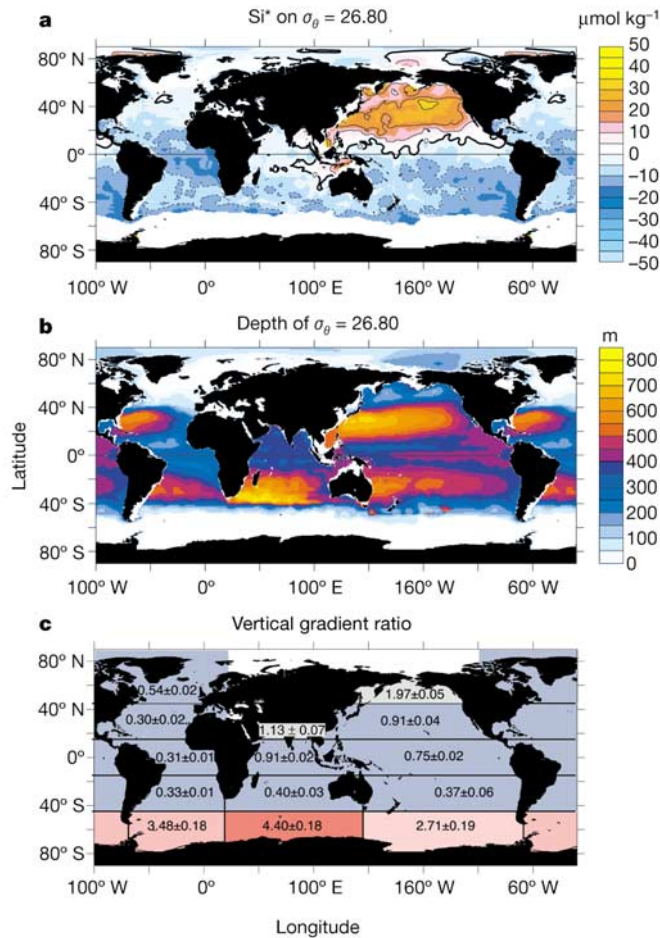
Figure 2 Global maps of nutrient properties mapped on the potential density surface $\sigma_\theta = 26.80$. The southern boundary is determined by where the annual mean density field outcrops at the surface of the ocean. **a**, Si*. See Methods section for discussion of evidence that Si* is conserved after the formation of SAMW in the SAZ. There are a few low-oxygen regions in the North Indian Ocean and eastern tropical Pacific where removal of nitrate as a consequence of denitrification decouples Si cycling from that of nitrate. We correct for this by using N* (ref. 30), to define a corrected Si* = Si(OH)$_4$ − NO$_3^-$ − δ(N*) where δ is set to one if N* is smaller than −2 μmol kg^{-1} and to zero otherwise. Si* is not conserved in the NPIW. **b**, Depth of the $\sigma_\theta = 26.80$ surface. The data for **a** and **b** are from ref. 28. **c**, The zonal mean of the ratio of the vertical gradient of silicic acid to that of nitrate between the surface 100 m and the next 100 m, calculated as described in the Methods section.

the Equator (Fig. 2a), where it accounts for 70% of the silicic acid supply for diatom production despite the fact that half the supply of nitrate comes from the Southern Hemisphere[16]. The influence of this water type can be seen at the surface of the ocean throughout the North Pacific, where the silicic acid to nitrate supply ratios are much higher than over the regions where SAMW influence dominates (Fig. 2c).

Model simulations in three-dimensional coupled biological–physical models consistently underpredict biological productivity in the North Pacific relative to observations[17]. This has been attributed to the failure to form NPIW with the right characteristics in these models[17]. Solving this problem may require developing a parameterization for the influence of tidally driven vertical mixing in the northwest Pacific.

There is also a modest amount of high-Si* water in the eastern equatorial Indian Ocean and Bay of Bengal (Fig. 2a), where the supply ratio to the surface is also large (Fig. 2c). The former
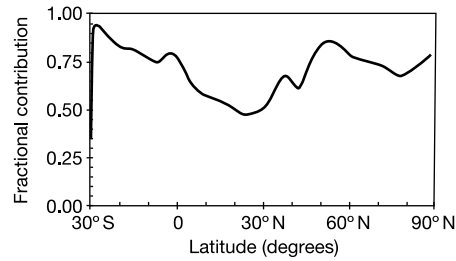

Figure 3 Predicted global zonal mean of the fractional contribution of Southern Ocean nutrient supply to global export production. Data obtained from an ocean biogeochemistry general circulation model (see model description in the Methods section). This figure is based on simulations carried out by R. Slater, with diagnostics provided courtesy of I. Marinov and A. Gnanadesikan.

probably results from North Pacific influence, but may also involve vertical mixing in the Indonesian Straits; the latter appears to be generated locally in the Bay of Bengal.

Given the importance of the SAMW and NPIW in the global thermocline nutrient cycle, we need to understand the processes that determine the properties of these water types. Previous work based on nitrogen isotopes suggests that surface nitrate in the SAZ and PFZ is carried northward by Ekman transport from the region to the south of the Polar Front[18], where upwelling brings water with extremely high nutrient concentrations to the surface of the Southern Ocean (Fig. 1a and b). Organisms in the upwelling zone utilize the nutrients as these waters move towards the north (Fig. 4). Figure 1c shows that the waters furthest to the south have Si* that goes as high as 50 μmol kg^{-1}, but by the time they reach the Polar Front they have Si* values of zero or less, with Si* becoming increasingly negative towards the north within the Polar Front Zone and Subantarctic Zone (Figs 1c and 4). The preferential removal of silicic acid that would be required in order to generate such decreases in Si* is a well known phenomenon (Fig. 2c), generally attributed to the influence of iron limitation in dramatically increasing the Si:N ratio of diatoms[19]. Studies in this region suggest that iron in sea ice and in upwelling deep water is sufficient to sustain intense diatom blooms but not high enough to prevent some manifestations of iron limitation, with the consequence that the Si:N ratio of diatoms is very high[20]. Lateral mixing along isopycnals from the interior of the ocean plays a role in determining the surface nutrient distribution in the Southern Ocean as well[21], but would not be able to provide the required upward supply of nutrients from the deep ocean to the SAMW formation region.

By contrast with the SAMW, the NPIW is rich in both nitrate and silicic acid. One might speculate that a difference in iron supply may play a role in mitigating the depletion of silicic acid relative to nitrate in this region. However, a more important contributor may be that NPIW formation, which occurs primarily by vertical mixing in the interior of the ocean, does not involve exposure at the surface of the ocean. The formation of NPIW thus avoids the biologically driven resetting of deep ocean nutrient ratios that occurs at the surface of the ocean during SAMW formation.

Our analysis has important implications for the impact of climate change on the global nutricline, biological productivity and the carbon cycle. The Southern Ocean has long been recognized as playing a central role in the global carbon cycle and biological productivity, and in the response of these to climate change[22,23]. We show that it is specifically the processes determining the properties of SAMW, and the mechanisms leading to its formation in the SAZ, that are most crucial in determining how Southern Ocean processes affect the supply of nutrients to the main thermocline and low-latitude productivity. The SAZ is a region of deep mixed layers;
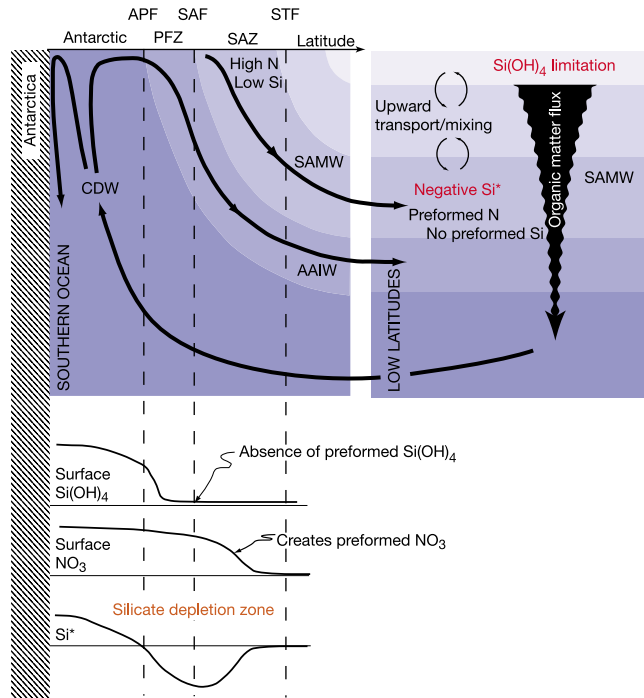
Figure 4 Southern Ocean control on thermocline nutrient concentrations. Conceptual diagram depicting the Southern Ocean physical and biological processes that form low-Si* waters and feed them into the global thermocline. Top, water pathways; bottom, details of surface processes. Upper Circumpolar Deep Water (CDW) upwells to the surface in the Southern Ocean, and is transported to the north across the Antarctic Polar Front (APF) into the Polar Front Zone (PFZ), where Antarctic Intermediate Water (AAIW) forms, and then across the Subantarctic Front (SAF) into the Subantarctic Zone (SAZ), which is bounded to the north by the Subtropical Front (STF). Silicic acid is stripped out preferentially over nitrate as the water moves to the north, thus generating negative Si* values. This negative-Si* water is Subantarctic Mode Water (SAMW), which sinks into the base of the main thermocline and feeds biological production in the low latitudes.

models and observations suggest that these layers are formed by a combination of cooling of subtropical gyre water and northward wind driven Ekman transport[24]. Both of these very probably changed during the ice ages and are likely to change with global warming, though the nature of the change is controversial. Our analysis also suggests that NPIW formation in the North Pacific is crucial in determining low-latitude productivity in the north and equatorial Pacific; NIPW formation thus merits greater attention than it has received in the past[10].

Methods

Conservation of Si*

The usefulness of preformed Si* as a tracer of the SAMW depends on the extent to which it is conserved. It will only be conserved if nitrate and silicic acid are recycled everywhere in a ratio of 1:1. Preferential remineralization of nitrate or of non-siliceous organisms, which is the behaviour that might be expected at the depth of the SAMW, will tend to reduce Si*. Figure 2a does not show any significant reduction of Si* away from the SAMW formation region, which provides qualitative support for conservation of this tracer.

We further examined this issue as follows. Both Si and N can be conceptually separated into preformed and remineralized components: $NO_{3_{Observed}}^- = NO_{3_{Preformed}}^- + \Delta NO_3^-$, and $Si(OH)_{4_{Observed}} = Si(OH)_{4_{Preformed}} + \Delta Si(OH)_4$. Combining these gives $Si^* = Si(OH)_{4_{Observed}} - NO_{3_{Observed}}^- = Si(OH)_{4_{Preformed}} - NO_{3_{Preformed}}^- + (\Delta Si(OH)_4 - \Delta NO_3^-)$. If remineralization were occurring with a 1:1 ratio, then $\Delta Si(OH)_4$ and ΔNO_3^- would be equal and $Si^* = Si(OH)_{4_{Preformed}} - NO_{3_{Preformed}}^-$. However, we expect some preferential remineralization of nitrate, so we further split ΔSi into a fraction that follows the 1:1 ratio and a term that contains the preferential remineralization, $\Delta Si(OH)_4 = \Delta Si(OH)_{4_{1:1}} + \Delta Si(OH)_{4_{Preferential}}$. However, $\Delta Si(OH)_{4_{1:1}} = \Delta NO_3^-$, so we have $Si^* = Si(OH)_{4_{Preformed}} - NO_{3_{Preformed}}^- + \Delta Si(OH)_{4_{Preferential}}$. On the $\sigma_\theta = 26.8$ surface, the preformed silicic acid concentration is close to 0, thus giving $\Delta Si(OH)_{4_{Preferential}} = Si^* + NO_{3_{Preformed}}^-$. We calculate preformed nitrate by subtracting the remineralized nitrate from the observed nitrate concentration,

$NO_{3_{Preformed}}^- = NO_{3_{Observed}}^- - \Delta NO_3^-$, with remineralized nitrate calculated from the apparent oxygen utilization ($AOU = O_{2_{Saturation}} - O_{2_{Observed}}$) multiplied by the average N:O$_2$ stoichiometric ratio of 16:170, that is, $\Delta NO_3^- = AOU \cdot 16/170$. Except for the large North Pacific signal, which has a different preformed concentration, a plot of the preferential silicic acid distribution on the $\sigma_\theta = 26.8$ surface is within $\pm 5 \mu mol\,kg^{-1}$ of 0, demonstrating that our assumption of minimal impact of preferential remineralization on the Si* distribution is a good one at the depth of the SAMW.

Export ratio

The opal to nitrogen export flux ratio is obtained from the water column nutrient data synthesis compiled from WOCE, SAVE, TTO and GEOSECS (see list of cruises in ref. 25); we used the method of ref. 25 to calculate the opal to organic carbon export flux ratio[25]. Briefly, ref. 25 shows how the export flux ratio can be calculated from the vertical concentration gradient ratio of the precursor inorganic nutrients if certain assumptions are met. As in that study, we calculate the concentration gradient ratio by taking the mean over the top 100 m for the surface concentration, and the mean over 100 to 200 m for the thermocline concentration. The 'most likely' export flux ratio is then obtained from

$$\left(\frac{J_{opal}}{J_{organic\;nitrogen}}\right) = \frac{\sum(\langle Si(OH)_4\rangle_{100-200\,m} - \langle Si(OH)_4\rangle_{0-100\,m})}{\sum(\langle NO_3^-\rangle_{100-200-m} - \langle NO_3^-\rangle_{0-100\,m})}$$

As in ref. 25, we use the bootstrap method to estimate the nonparametric standard deviation of the mean. We construct 10,000 trial data sets from the original data set by random selection with replacement (that is, repeatedly randomly selecting from the same set of observations). The 'best' estimate of the gradient is the median of all the individual estimates, and the 95% confidence limits come directly from the 2.5% and 97.5% tails of the resulting distribution.

Contribution of Southern Ocean to export production

The model simulations of the influence of the Southern Ocean on ocean biological production are carried out in the KVLOW + AILOW ocean biogeochemical general circulation model discussed in ref. 17. Biological uptake of nutrients is obtained by forcing model predicted nutrients towards observed nutrients in the upper 75 m of the model. The model includes production and remineralization of both dissolved and particulate organic matter. We shut off the Southern Ocean nutrient supply to low latitudes by forcing surface nutrients towards zero south of 30° S such that the water sinking out of the surface has little or no nutrients in it. We note that the results we obtain are very sensitive to the model used, and that we forced nutrients towards zero everywhere south of 30° S, not just in the SAMW formation regions.

1. Toggweiler, J. R. & Samuels, B. in *The Global Carbon Cycle* (ed. Heimann, M.) 333–366 (Springer, Berlin, 1993).
2. McCartney, M. S. The subtropical recirculation of mode waters. *J. Mar. Res.* **40** (suppl.), 427–464 (1982).
3. Sloyan, B. M. & Rintoul, S. R. Circulation, renewal, and modification of Antarctic Mode and Intermediate Water. *J. Phys. Oceanogr.* **31**, 1005–1030 (2001).
4. Talley, L. D. An Okhotsk Sea water anomaly: Implications for ventilation in the North Pacific. *Deep-Sea Res.* **38** (suppl. 1), S171–S190 (1991).
5. Ledwell, J. R., Watson, A. J. & Law, C. S. Evidence for slow mixing across the pycnocline from an open-ocean tracer-release experiment. *Nature* **364**, 701–703 (1993).
6. Toggweiler, J. R., Dixon, K. & Broecker, W. S. The Peru upwelling and the ventilation of the South Pacific thermocline. *J. Geophys. Res.* **96**, 20467–20497 (1991).
7. McCartney, M. S. in *A Voyage of Discovery* (ed. Angel, M. V.) 103–119 (Supplement to Deep-Sea Research, George Deacon 70th Anniversary Volume, Pergamon, Oxford, 1977).
8. Hanawa, K. & Talley, L. D. in *Ocean Circulation and Climate* (eds Siedler, G. & Church, J.) 373–386 (Academic, San Diego, 2001).
9. Ragueneau, O. *et al.* A review of the Si cycle in the modern ocean: Recent progress and missing gaps in the application of biogenic opal as a paleoproductivity proxy. *Glob. Planet. Change* **26**, 317–365 (2000).
10. Tsunogai, S. The Western North Pacific playing a key role in global biogeochemical cycles. *J. Oceanogr.* **58**, 245–257 (2002).
11. Reid, J. L. On the total geostrophic circulation of the Pacific Ocean: Flow patterns, tracers, and transport. *Prog. Oceanog.* **29**, 263–352 (1997).
12. Talley, L. D. North Pacific Intermediate Water transports in the mixed water region. *J. Phys. Oceanogr.* **27**, 1795–1803 (1997).
13. Yasuda, I., Kouketsu, S., Katsumata, K. & Ohiwa, M. Influence of Okhotsk Sea Intermediate Water on the Oyashio and North Pacific Intermediate Water. *J. Geophys. Res.* **107**, doi:10.1029/2001JC001037 (2002).
14. Nakamura, T. *et al.* The generation of large-amplitude unsteady lee waves by subinertial K_1 tidal flow: A possible vertical mixing mechanism in the Kuril Straits. *J. Phys. Oceanogr.* **30**, 1601–1621 (2000).
15. Yasuda, I. *et al.* Hydrographic structure and transport of the Oyashio south of Hokkaido and the formation of North Pacific Intermediate Water. *J. Geophys. Res.* **106**, 6931–6942 (2001).
16. Dugdale, R. C. *et al.* Meridional asymmetry of source nutrients to the equatorial Pacific upwelling ecosystem and its potential impact on ocean-atmosphere CO$_2$ flux; a data and modeling approach. *Deep-Sea Res. II* **49**, 2513–2531 (2002).
17. Gnanadesikan, A., Slater, R. D., Gruber, N. & Sarmiento, J. L. Oceanic vertical exchange and new production: A comparison between models and observations. *Deep-Sea Res. II* **49**, 363–401 (2002).
18. Sigman, D. M., Altabet, M. A., McCorkle, D. C., Francois, R. & Fischer, G. The $\delta^{15}N$ of nitrate in the Southern Ocean: Consumption of nitrate in surface waters. *Glob. Biogeochem. Cycles* **13**, 1149–1166 (1999).
19. Franck, V. M., Brzezinski, M. A., Coale, K. H. & Nelson, D. M. Iron and silicic acid concentrations regulate Si uptake north and south of the Polar Frontal Zone in the Pacific Sector of the Southern Ocean. *Deep-Sea Res. II* **47**, 3315–3338 (2000).

59

letters to nature

20. Brzezinski, M. A., Dickson, M.-L., Nelson, D. M. & Sambrotto, R. Ratios of Si, C and N uptake by microplankton in the Southern Ocean. *Deep-Sea Res. II* **50**, 619–633 (2003).
21. Pollard, R. T., Lucas, M. I. & Read, J. F. Physical controls on biogeochemical zonation in the Southern Ocean. *Deep-Sea Res. II* **49**, 3289–3305 (2002).
22. Sarmiento, J. L., Hughes, T. M. C., Stouffer, R. J. & Manabe, S. Simulated response of the ocean carbon cycle to anthropogenic climate warming. *Nature* **393**, 245–249 (1998).
23. Sigman, D. M. & Boyle, E. A. Glacial/interglacial variations in atmospheric carbon dioxide. *Nature* **407**, 859–869 (2000).
24. Speer, K., Rintoul, S. R. & Sloyan, B. The diabatic Deacon Cell. *J. Phys. Oceanogr.* **30**, 3212–3222 (2000).
25. Sarmiento, J. L. *et al.* A new estimate of the CaCO₃ to organic carbon export ratio. *Glob. Biogeochem. Cycles* **16**, doi:1029/2002GB00191 (2002).
26. Moore, J. K., Abbott, M. R. & Richman, J. G. Location and dynamics of the Antarctic Polar Front from satellite sea surface temperature data. *J. Geophys. Res.* **104**, 3059–3073 (1999).
27. Belkin, I. M. & Gordon, A. L. Southern Ocean fronts from the Greenwich meridian to Tasmania. *J. Geophys. Res.* **101**, 3675–3696 (1996).
28. Levitus, S. *et al. World Ocean Database 1998* Vol. 1, *Introduction* (NOAA NESDIS, Washington DC, 1998).
29. Kara, A. B., Rochford, P. A. & Hurlburt, H. E. Mixed layer depth variability over the global ocean. *J. Geophys. Res.* **108**, doi:10.1029/2000C000736 (2003).
30. Gruber, N. & Sarmiento, J. L. Global patterns of marine nitrogen fixation and denitrification. *Glob. Biogeochem. Cycles* **11**, 235–266 (1997).

····························

Stability of magnesite and its high-pressure form in the lowermost mantle

Maiko Isshiki[1,2]**, Tetsuo Irifune**[1]**, Kei Hirose**[3]**, Shigeaki Ono**[4]**, Yasuo Ohishi**[2]**, Tetsu Watanuki**[5]**, Eiji Nishibori**[6]**, Masaki Takata**[2,6] **& Makoto Sakata**[6]

[1]*Geodynamics Research Center, Ehime University, Matsuyama, Ehime 790-8577, Japan*
[2]*SPring-8/Japan Synchrotron Radiation Research Institute, 1-1-1 Kouto, Mikazuki, Sayo, Hyogo 679-5148, Japan*
[3]*Department of Earth and Planetary Sciences, Tokyo Institute of Technology, 2-12-1 Ookayama, Tokyo 152-8551, Japan*
[4]*IFREE, Japan Marine Science & Technology Center, 2-15 Natsushima, Yokosuka, Kanagawa 237-0061, Japan*
[5]*SPring-8/Japan Atomic Energy Research Institute, 1-1-1 Kouto, Mikazuki, Sayo, Hyogo 679-5148, Japan*
[6]*Department of Applied Physics, Nagoya University, Furo-cho, Chikusa, Nagoya 464-8603, Japan*

···

Carbonates are important constituents of marine sediments and play a fundamental role in the recycling of carbon into the Earth's deep interior via subduction of oceanic crust and sediments[1–3]**. Study of the stability of carbonates under high pressure and temperature is thus important for modelling the carbon budget in the entire Earth system. Such studies, however, have rarely been performed under appropriate lower-mantle conditions and no experimental data exist at pressures greater than 80 GPa (refs 3–6). Here we report an *in situ* X-ray diffraction study of the stability of magnesite (MgCO₃), which is the major component of subducted carbonates, at pressure and temperature conditions**

approaching those of the core–mantle boundary. We found that magnesite transforms to an unknown form at pressures above ~115 GPa and temperatures of 2,100–2,200 K (depths of ~2,600 km) without any dissociation, suggesting that magnesite and its high-pressure form may be the major hosts for carbon throughout most parts of the Earth's lower mantle.

In equilibrium with silicates, the major carbonates in marine sediments (CaCO₃ calcite, CaCO₃ aragonite, and CaMg(CO₃)₂ dolomite) transform to dolomite and magnesite with increasing pressure to ~1–4 GPa (refs 7, 8), depending on temperature and bulk compositions. Dolomite has been shown to transform further, to magnesite-bearing assemblages in the presence of pyroxene and olivine at pressures of 20–50 GPa (ref. 3): accordingly, magnesite should be the only stable carbonate in the upper part of the mantle. Direct evidence of the presence of magnesite has also been demonstrated by its occurrence as inclusions in natural diamonds[9], although it has been a matter of debate whether it is transported into the lower mantle via subduction[3,10,11].

The stability of MgCO₃ magnesite under lower-mantle conditions has been studied by using the diamond anvil cell (DAC); these studies showed that magnesite is stable at pressures to 80 GPa and temperatures of 2,000–2,500 K (refs 3–6). However, these studies were based on analyses of samples quenched to ambient conditions, or those at room temperature under high pressure, except for one study using Raman spectroscopy at 26 GPa and at 1,200 K (ref. 5), and no *in situ* X-ray diffraction studies under simultaneous high pressure and high temperature have been made. Moreover, the temperatures in most of these experiments were only poorly constrained and suffered large uncertainties (10–20% of the nominal values), and in some studies they were not even measured[3,4]. The maximum pressures studied were also limited to 50–80 GPa, equivalent to depths of ~1,300–1,900 km in the mantle, and so the stability of magnesite throughout the mantle remains unresolved.

We made 12 runs of *in situ* X-ray measurements at high pressure and temperature, as summarized in Table 1. In each run, X-ray diffraction measurements were conducted at two or three different pressure–temperature conditions by increasing temperature at a fixed load. Magnesite was found to persist to pressures up to about 100 GPa, and at temperatures up to 3,000 K, and we did not see any evidence for the dissociation of MgCO₃ under these conditions (Fig. 1a–c). The unit-cell volume of magnesite was determined at high pressure after quenching to room temperature in each run. A least-squares fitting of

Table 1 Experimental conditions and results

Run number	P (GPa)	T (K)	t (min)	Results
Ms29	30.7	1,800	5	Magnesite
	30.2	2,300	5	Magnesite
Ms26	38.8	1,800	5	Magnesite
	41.8	2,200	5	Magnesite
Ms28	47.8	2,000	5	Magnesite
	50.9	2,500	5	Magnesite
Ms23	51.6	1,800	5	Magnesite
	54.8	2,200	5	Magnesite
	55.4	2,500	5	Magnesite
Ms7	59.1	1,800	5	Magnesite
	60.6	2,000	5	Magnesite
Ms22	62.5	1,800	5	Magnesite
Ms25	66.1	1,800	5	Magnesite
	63.0	2,400	5	Magnesite
Ms8	78.0	1,800	3	Magnesite
	81.6	2,500	3	Magnesite
	84.3	3,000	3	Magnesite
Ms16	96.9	2,000	10	Magnesite
Ms14	100.8	1,800	5	Magnesite
	100.1	2,200	5	Magnesite
Ms15	112.6	1,800	5	Magnesite
	114.4	2,200	5	Magnesite II (+magnesite)
Ms18*	116.3	2,100	10	Magnesite II (+magnesite)

*Al₂O₃ pressure medium was not used.